Potassium-Promoted Three-Dimensional Mesoporous Pt/MnO_2 for Formaldehyde Elimination at Zero Degree

Shengnan Guan, Wenzhi Li*, Jianru Ma, Qingchuan Liu, Kun Chen and Qi Zhang
[1]*Basic Research Laboratory for Biomass Conversion，Department of Thermal Science and Energy Engineering, School of Engineering Science, University of Science and Technology of China, Hefei 230026, Anhui, China*
[2]*Hefei University of Technology, School of Biological and Medical Engineering, No.193 Tunxi Road, Baohe District, Hefei, Anhui 230009, PR China.*
[3]*CAS Key Laboratory of Renewable Energy, Guangzhou Institute of Energy Conversion, Chinese Academy of Sciences, Guangzhou 510640, PR China.*
liwenzhi@ustc.edu.cn*

(Received on 30th November 2018, accepted in revised form 17th May 2019)

Summary: In this work, three-dimensional mesoporous MnO_2, K/MnO_2, Pt/MnO_2 and K-Pt/MnO_2 catalysts were prepared through hard-template method. The additional K/Pt had significantly improved the HCHO oxidation activity. The K-Pt/MnO_2 catalyzed complete HCHO oxidation was achieved at 0°C with space velocity (GHSV) at 50000 ml/(g·h). With the excellent catalytic performance, K-Pt/MnO_2 exhibited a higher ratio of O_{ads}(surface adsorbed oxygen)/O_{latt}(surface lattice oxygen) and Mn^{3+}/Mn^{4+} ions than the other catalysts. Meanwhile, it was still stable after running a 70h reaction. Overall, the K-Pt/MnO_2 was a promising material for HCHO elimination.

Keywords: Low-temperature; Formaldehyde oxidation; K/Pt-promoted; Catalytic Activity； Environment

Introduction

Formaldehyde is an air and photochemical pollutant that emitted from the decorative and building materials such as coatings and textiles [1]. As one of the most dominant room air pollutants [2], a long-term breathing of even few parts per million of formaldehyde could lead to health hazard. Thus, great efforts have been made around formaldehyde elimination in order to satisfy stringent environment regulations [3,4]. Conventional methods of formaldehyde removal include plasma technology, adsorption, photo-catalysis and catalytic oxidation [5-7]. Catalytic oxidation was proved as an efficient and economic technique for removal of formaldehyde since it can convert the volatile organic compounds into CO_2 and H_2O in relatively low temperatures [8-10]. The key to formaldehyde catalytic oxidation is the development of high efficient catalysts.

As formaldehyde catalytic oxidation at even lower temperatures is worthwhile for indoor air purification, the mainly noble metal catalysts for formaldehyde combustion, for example, platinum supported by MnO_2-CeO_2 [3], TiO_2 [11,12], MnO_x [13], and gold supported by CeO_2 [14-16], Co_3O_4-CeO_2 [17], CeO_2-Co_3O_4 [18], have been intensively researched due to their prominent activity and stability at low catalytic temperatures. Among them, Platinum (Pt) catalysts exhibit superior formaldehyde decomposition catalytic performance even at ambient temperature. There also have maken some efforts for the study of transition metal-oxides [19], such as MnO_2 [20], TiO_2 [21], Co_3O_4 [22]. Among these transition metal oxides, MnO_2 recently represents its potential as a prospective material used for energy storage, water oxidation and pollution abatement [23-25], and Mn based catalysts is widely researched because of their superior catalytic activity towards formaldehyde oxidation [26]. Compared with the pure transition metal oxides mentioned above, precious metal samples supported by oxide can supply abundant active sites to formaldehyde catalytic reaction. The interaction between support with precious metal has been demonstrated to play a highly favorable effect on HCHO oxidation performance [27-29]. Yan [30] attached platinum on nanorod-shaped Co_3O_4 by calcination of cobaltosic oxide precursor before the sodium borohydride reduction of platinum precursor. The Co_3O_4 catalyst contained platinum showed an outstanding performance for formaldehyde removal at ambient temperature, which to a large extent because of the strong support-metal interaction between Co_3O_4 and Pt. Min Wang *et al.*,.[31] prepared Pt/MnO_2 catalyst with 2wt% Pt by method of ascorbic acid reduction [32] that the platinum nano-particles(2 nm) were highly dispersed on manganese dioxide. As-prepared catalyst Pt/MnO_2 demonstrated a remarkably enhanced catalytic activity, which kept eliminating

*To whom all correspondence should be addressed.

C_2H_4 (20 ppm) completely at 50°C for at least 12h. The increscent amount of O_{ads} species on Pt/MnO_2 contributed to its excellent property for C_2H_4 oxidation. Moreover, the support–metal interaction between MnO_2 and Pt played a role in promoting the performance of MnO_2 contained platinum catalyst. These studies provided new enlightenments into the preparation of high-performance catalysts for HCHO oxidation.

Hydroxyl radical(OH-) is a strong oxidizing agent in the nature. There is a certain amount of water in the air, and the alkali salts could convert water to hydroxyl radical under the proper condition, which enhances the concentration of hydroxide radical and the adsorption property of formaldehyde [35,36]. The adsorption/activation of HCHO is a critical process, which -OH bonded with the samples surface for formaldehyde elimination [33,34]. Some strategies have been applied to strengthen the interaction between catalytic surface and HCHO, and adding alkali metal salts into the supported catalysts is one important method. For instance, Nie *et al.,*.[37] found that adding sodium ions into TiO_2 contained Pt can enhance the formaldehyde oxidation performance. Avgouropoulos[38] compared K-Pt/Al_2O_3 and Na-promoted Pt/Al_2O_3 catalyst, and found that K-Pt/Al_2O_3 could promote the C_2H_5OH catalytic oxidation preferably. Hou[39] discovered that the addition of potassium ion could promote O^{n-} activity of the catalysts. The facilitation of potassium ion has also been found over hollandite manganese oxide in HCHO oxidation. Zhang[40] interpreted potassium ion effect from other perspective. The Na--promoted Pt-O-$(OH)_x$ catalysts which was atom-dispersed could stimulate water efficiently, and promote facile reaction within $HCOO^-$ and surface OH species to CO_2 and H_2O. This similar phenomenons were also found in Na-Pd/TiO_2 and K-Ag-MnO_2 catalysts[41]. Thus, those successful alkali modified catalysts stimulated us to apply a similar modification to the catalyst that was used for room-temperature formaldehyde catalytic oxidation.

Mesoporous metal oxides has been attached great importance due to their specific pore structure, controllable pore diameter, great surface area[42-47] and their pore structure that can fully contact with the reactant gas. VOCs catalytic oxidation over 3D-MnO_2 showed the potential availability. It had remarkable hydrophobicity, a strong affinity toward volatile organic compounds, and it also can selectively adsorb volatile organic compound molecules[48]. So, the 3D-MnO_2 was chosen as the basic framework for formaldehyde oxidation catalyst modification.

In this research, the mesoporous Pt/MnO_2 sample was synthesized by the impregnation method. The K−Pt/MnO_2 catalyst was prepared by adding potassium ions to Pt/MnO_2. The interaction between the precious metal and carriers, oxygen species, changes in the valence state of the carriers surface elements and lattice defects on catalytic performance were investigated[49,50]. As-prepared K−Pt/MnO_2 catalysts exhibited enhanced catalytic performance for the formaldehyde oxidation as well as better stability. For purpose of finding out the relationship between catalysts performance and structure, the samples were characterized by XRD, SEM, TEM, BET, FTIR spectra, XPS, Raman, H_2 -TPR, O_2-TPO, and their formaldehyde catalytic performance was assessed as well.

Experimental

Material preparation

Tetraethoxysilane (SiO_2≥28.4%, AR), hydrochloric acid (36.0~38.0%, AR), n-butanol (purity≥99%, AR), $Mn(NO_3)_2{\cdot}4H_2O$ (97.5%), H_2O_2 (purity≥30%, AR), K_2CO_3 (purity≥99%, AR), NaOH (purity≥96%, AR), and sodium citrate (purity≥99%, AR) were purchased from Sinopharm Chemical Reagent Company, Limited (Shanghai). Pluronic P123 ($EO_{20}PO_{70}EO_{20}$), and $PtCl_4$ (99.9%, metals basis) were purchased from Aladdin in China. All the materials were AR grade and employed without purification in degree.

Using the silica source-tetraethoxysilane (TEOS) and the structure-directing agent-Pluronic P123 ($EO_{20}PO_{70}EO_{20}$) to synthesize cubic Ia3d SiO_2. In a conventional preparation, P123 (7.2 g, 1.2 mmol), n-butanol (7.0 g, 94.5 mmol) and HCl (13.9 g, 37%) were put into the round flask(500 ml), then stirred for an hour[51]. During synthesis process, the temperature was maintained at 38°C. The liquor was agitated for an additional twenty four hours after tetraethoxysilane (7.0 g) was added. The liquor was moved to a Teflon-lined autoclave, then kept for twenty four hours at 100°C. After the hydrothermal treatment, the liquid was filtered a few times using deionized water. To completely remove the template, the sample was calcined at 550°C for 5 hours after drying at 100°C. The white 3D-cubic KIT-6 (ia3d) mesoporous material was obtained.

The nanocasting preparation of mesoporous

3D-MnO_2[42] was started at adding 4.0 g KIT-6 molecular sieve into 40 mL $Mn(NO_3)_2{\cdot}4H_2O$ in alcohol (0.91 mol/L). It was dried in drying oven at 80℃ before calcining at 200℃ for 6 hours. The above-mentioned casting and drying steps were done again. Then, the sample was calcined at 400℃ for 6 hours with a heat rate of 5℃/min under air. The KIT-6 was eliminated through the NaOH solution (2 mol/L). After removing sodium silicate using centrifugal separation, the obtained precipitate was dried at 100℃, and calcined at 400℃.

Adding 1.5 g as-prepared MnO_2 into deionized water(10 mL) which was added to 1.1 g K_2CO_3 to yield K/MnO_2 catalyst[41], which proved to be effective of this quantity. Then, adding 22.7 ml H_2O_2 solution into MnO_2 solution dropwise during stirring. The solution kept stirring for another 1 hour and centrifuged（8000 rpm） to separate the solid from liquid phase. The sample was desiccated in oven at 110℃, then calcined at 500℃ for 4 hours.

MnO_2(0.3 g) was added into deionized water(10 mL) to yield Pt/MnO_2. During stirring, adding 0.0154mmol $PtCl_4$ (dissolved in ~350μL 0.1M HCl) make the platinum coming to 1 wt%. Then, 5 mL of sodium citrate (1 mM) and $NaBH_4$ (0.572 M) mixture was added quickly, and stirred for 300 min. Then, the samples were filtered through centrifugation using purified water. The washed powder was dried overnight at 60℃ which denoted as Pt/MnO_2. Preparation of K-Pt/MnO_2 samples was similar to Pt/MnO_2. After adding H_2PtCl_6 solution, 0.22 g K_2CO_3 was added immediately to obtain the K-Pt/MnO_2 catalyst.

Material characterization

XRD analyse was performed on the smartlab type X-ray diffractometer (Japan) utilizing the Cu Kα radiation source with a 40 mA tube current, 40 kV tube voltage and 0.05°/min scanning speed. The 2θ of wide-angle XRD was ranged from 20°to 80°, respectively. Nitrogen adsorption/desorption experiment was performed on an Autosorb-Tristar II 3020M apparatus (Micromeritics inc). All catalysts were degassed at 300℃ for 4h under vacuum before the measurement. The Nitrogen adsorption-desorption isotherms were measured using the Barrett-Joyner-Halenda method. The Scanning Electron Microscope analyses were performed on a XL-30 ESEM apparatus (FEI Electronics Optics Corporation) at a voltage of 5.0 and 30 kV. The catalyst was prepared by ultrasonic waves dispersing in alcohol for 5 min and placed on a lacey carbon film. The Transmission electron microscopy images were performed on a JEM-2100F apparatus (JEOL) at an accelerating voltage of 200 kV. The catalysts were also dispersed by ultrasonic in ethanol for 5 min, and the droplets were put on the copper grid using capillaries. Fourier-transform infrared spectra were measured in the range from 400 to 4000 cm^{-1} at a resolution of 4cm^{-1} on the Nicolet 8700 FT-IR spectrometer (American Thermo Nicolet instrument co.). Temperature programmed measurements in this work include the temperature programmed reduction experiments (TPR) and temperature programmed oxidation experiments (TPO). The H_2-TPR was carried out in the Quantachrome 1900 instrument. Four kinds of catalysts (0.15g) were placed in a U-shaped quartz tube, and pretreated in nitrogen flow at 300℃ for 1 h. After that, the catalysts were cooled and reduced in 10% H_2 and 90% Ar flow (50mL/min) using a temperature range from 30℃ to 900℃ at 10℃/min. The H_2 consumptions were calculated by the integrated TPR peaks area, and calibrated by a CuO (99.998%) standard sample. TPO experiments were also performed on this instrument. The catalyst was pretreated in He flow at 300℃, after that, they were oxidized in 4% O2 /He flow at programmed temperature range of 50-700℃ with a rate of 10℃/min. The XPS analysis was performed on a ESCALAB 250 instrument (Thermo-VG Scientific) with Mg Ka X-rays source, operating at 300 W. The carbon peak C 1s at a binding energy of 284.6 eV was used as the reference in order to correct the effect of electric charge. The peak areas processed was conducted using the XPS-PEAK software, and the ratio of elements with different chemical valence was computed. Laser Raman spectra were recorded on a LabRam-HR spectrometer (JY, France) using Ar^+ laser (514.5 nm) and He Cd lasers (325 nm) as the excitation source.

Catalytic activity tests

The HCHO oxidation reaction was performed in a quartz fixed-bed tube reactor (φ3 mm) with 60mg of catalyst (in powder). The total flow rate of the gas (20 ppm HCHO, 20% (vol) O_2, and N_2 gas) was maintained at 50 mL/min with the GHSV of 50,000 ml/(g·h). The relative humidity maintained at about 50%. Immersing the quartz tube in the freezer containing refrigerating fluid for the catalytic reaction below room temperature. The outlet formaldehyde was analyzed online by an Kexiao 1690 gas chromatograph equipped with a FID

detector and the PQ column. Reaction at each temperature point took eight minutes. Since the outlet and inlet concentration of formaldehyde varied to some extent, they were recorded for three times. The formaldehyde efficiency was calculated as follows:

$$\text{HCHO conversion}(\%) = \frac{[\text{HCHO}]_{in} - [\text{HCHO}]_{out}}{[\text{HCHO}]_{in}} \times 100\%$$

where $[HCHO]_{in}$ and $[HCHO]_{out}$ are the inlet HCHO concentration and the outlet HCHO concentration. The reaction rates (RT) of catalysts for formaldehyde removal at different temperatures were performed. T was the reaction temperature(°C). The reaction rate, RT ($mol \cdot m^{-2} \cdot s^{-1}$) was obtained through $RT = C_{HCHO} \cdot N_{HCHO}/A$, where C_{HCHO} on behalf of HCHO conversion, N_{HCHO} represented the molar-flow-rate (mol/s) of HCHO and A represented surface area (m^2).

Results and Discussion

Textural and structural characterization

The XRD patterns of MnO_2, K/MnO_2, Pt/MnO_2 and $K\text{-}Pt/MnO_2$ were presented in Fig.1. The peaks of all the materials located around 28.7°(1 1 0), 37.3°(1 0 1), 42.8° (1 1 1), 56.7°(2 1 1), 59.4°(2 2 0), 64.8°(0 0 2) and 72.3°(301). The reflections of the samples attributed to the β-MnO_2 crystal phase that according with pyrolusite with rutile structure[52,53]. No accessional peaks concerned with the loaded platinum were found, manifesting that the platinum grain size could be little and good dispersed. TEM patterns of Pt/MnO_2 and $K\text{-}Pt/MnO_2$ were exhibited in the later section of this paper. It was seen that the loaded platinum nano-particles with high dispersion were in the range from 2nm to 3nm.

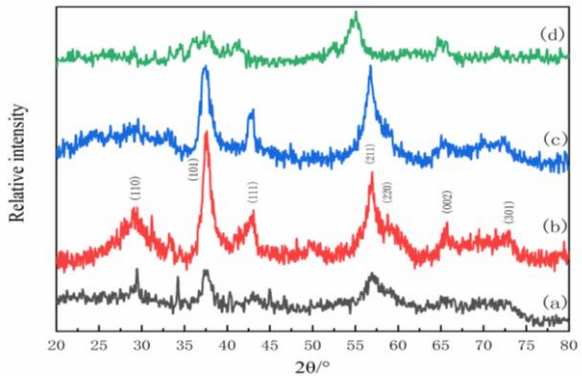

Fig.1: The XRD patterns of MnO_2 (a), K/MnO_2 (b), Pt/MnO_2 (c) and $K\text{-}Pt/MnO_2$ (d).

Fig.2 showed the N_2 adsorption/desorption patterns and average pore diameters of MnO_2, K/MnO_2, Pt/MnO_2 and $K\text{-}Pt/MnO_2$. All the N_2 adsorption/desorption patterns had hysteresis rings which identified as type IV[54-59], which attributing to the existence of interconnected mesopores with some constriction. The decrease in the hysteresis rings for K/MnO_2, Pt/MnO_2 and $K-Pt/MnO_2$ showed in Table-1 might be in connection with the decrease of the surface areas. The BJH pore size distribution that was obtained through the desorption isotherm was showed in Fig.2(inset). The pore diameter of MnO_2 was 3.8nm at a maximum distribution. The $K\text{-}MnO_2$ showed pore size of 1.9nm at a maximum distribution, the $Pt\text{-}MnO_2$ shows 2.7nm, 3.0nm and 3.8nm at maximum distributions, and $K\text{-}Pt/MnO_2$ shows 2.7nm at a maximum distribution, respectively. The replication of their KIT-6 templates resulted in the pore properties of the catalysts. After removing template, the crystallite regions made up of bulk silica and the regions made up of MnO_2 became the pore channels and the crystalline walls, respectively. Table-1 listed the physical parameters of all four samples. The smallest specific surface area was 41 m^2/g for $K\text{-}Pt/MnO_2$. The BET were 53 m^2/g and 81 m^2/g for $K\text{-}MnO_2$ and $Pt\text{-}MnO_2$, which had smaller BET and pore volumes than MnO_2. The pore diameters and surface areas of catalysts decreased with the addition of K/Pt. As the table was showed, the BET of catalysts decreased with the doping of K/Pt content. The BET surface area of $K\text{-}Pt/MnO_2$ was reduced which probably due to the reason that platinum nanoparticles and K^+ might overlay the MnO_2 surface and cover pores partially. The pore volume of Pt/MnO_2 was drastic increased, which could originate from adding H_2PtCl_6 solution during the preparation for Pt/MnO_2 catalysts. As a result of the corrosion, there were holes with diameter dimensions from dozens or even hundreds of nanometers. When the hard template was eliminated, the mesoporous MnO_2 lost part of the structure. The following SEM patterns presented the missing structure which was made up of incompletely removed SiO_2.

Fig. 3 presented the surface structure of mesoporous SiO_2, MnO_2, K/MnO_2, Pt/MnO_2 and $K\text{-}Pt/MnO_2$. All samples clearly exhibited 3D ordered mesoporous structures. The SEM images of MnO_2 were shown in Fig.3b,c. These images clearly showed MnO_2 possesses an ordered pore channel structure. The MnO_2 catalyst had a symmetrical 3D double pore channel structure because of the perfect replication of KIT-6 template.

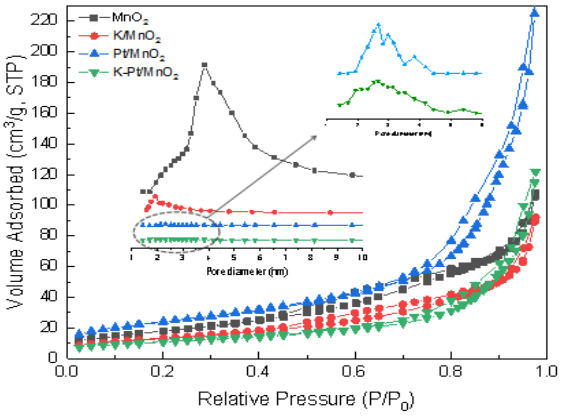

Fig. 2: N_2 adsorption/desorption isotherms and the corresponding pore size distributions of MnO_2, K-MnO_2, Pt-MnO_2 and K-Pt/MnO_2.

Table-1: Physical parameters and bulk composition of different catalysts.

Sample	Surface areas[a]	Pore volumes	Pore diameters[b]	Surface element molar ratio[c]	
	A_{BET} (m^2/g)	V_p (cm^3/g)	D_P(nm)	Mn^{3+}/Mn^{4+}	O_{ads}/O_{latt}
MnO_2	86	0.17	3.8	0.52	1.18
K/MnO_2	53	0.14	1.9	0.89	1.27
Pt/MnO_2	81	0.36	2.7/3.0/3.8	1	1.67
K-Pt/MnO_2	41	0.19	2.7	1.08	2

a Specific surface areas calculated by the Brunauer–Emmett–Teller method.
b Pore diameters obtained from the nitrogen adsorption isotherms by the Barrett-Joyner-Halenda method.
c Surface element molar ratio determined by the XPS measurement.

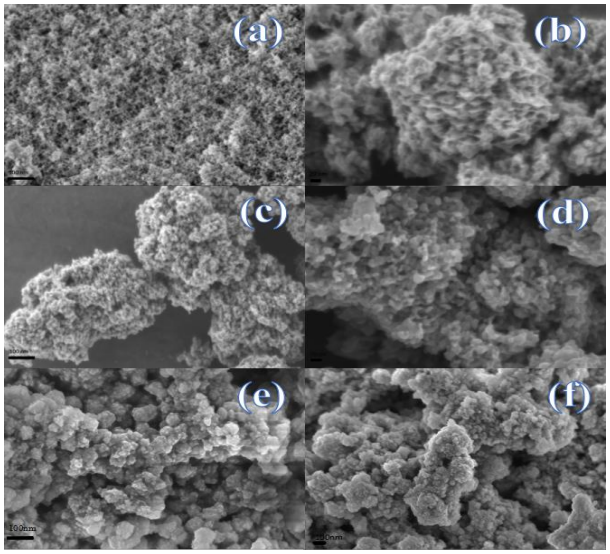

Fig.3: SEM image of KIT-6 (a), MnO_2 (b,c), K-MnO_2 (d), Pt-MnO_2 (e) and K-Pt/MnO_2 (f)

Fig 4 clearly displayed that all the catalyst samples were possessed an ordered mesoporous characteristics and polycrystalline walls. MnO_2 possessed a 3D mesoporous structure (Fig 4b). The thicken crystalline walls and narrow pore diameters were showed with the presence of Pt in catalyst. Compared with MnO_2, Pt/MnO_2 and K-Pt/MnO_2, all of catalysts showed homogeneous distribution of platinum NPs on surface of the polycrystalline walls, which is consistent with SEM results. Although many "black balls" were exhibited in the TEM images (Fig. 4a) of KIT-6, they were probably the skeleton intersections that were viewed along the [111] or [100] direction according to the structure analysis of MnO_2 in other researcher's literature [60]. Except for the skeleton intersections, smaller "black balls" illustrated the platinum NPs on surface of MnO_2 catalysts. Some platinum NPs were also dispersed on the skeleton intersections. According to Fig 4d, e and f, the Pt/MnO_2 and K-Pt/MnO_2 had about 2~3 nm Pt nanoarticles .

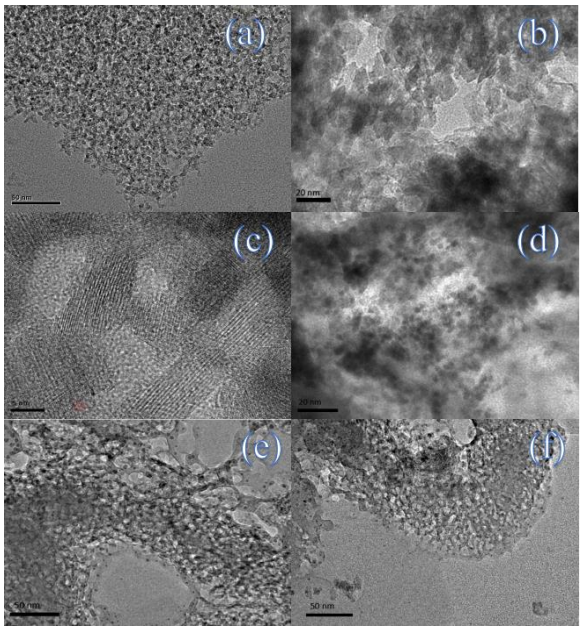

Fig. 4: TEM images of KIT-6 (a), MnO_2 (b),K-MnO_2 (c),Pt-MnO_2 (d) and K-Pt/MnO_2 (e,f).

The existence of OH- groups on surface of the catalysts was further verified by the FT-IR spectra. Fig. 5 exhibited similar FTIR spectra for MnO_2, K/MnO_2, Pt/MnO_2 and K-Pt/MnO_2. Absorption bands that located at 3410 and 1638 cm^{-1} assigned to stretching and bending vibrations of hydrogen bounded OH-, respectively [61]. The OH- groups on

the catalysts surface were beneficial for formaldehyde removal, according to the previous studies [62-64]. The bands ranged from 400 cm^{-1} to 800 cm^{-1} were identified as Mn-O band vibrations[65]. Because of the displacement of the oxygen anions, the absorption band at 559 cm^{-1} was observed attributed to the vibration, which assigned to the Mn ions together with the direction of the octahedral chains. The MnO_6 stretching mode octahedral together with the double-chain absorption band was centered at 705 cm^{-1}.

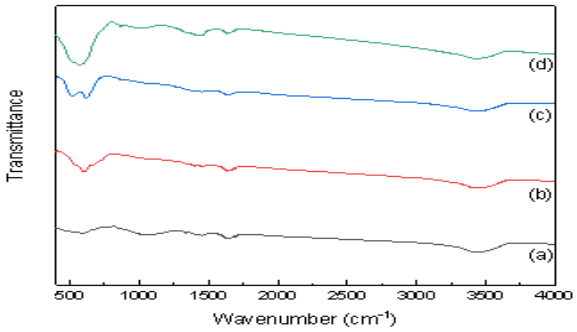

Fig.5: FTIR spectra of MnO_2 (a),K/MnO_2 (b),Pt/MnO_2 (c) and $K\text{-}Pt/MnO_2$ (d).

Chemical Characterization

In Fig 6A, the binding energy at ~641.8 eV and ~643 eV were attributed to two components of Mn $2p_{2/3}$, which separately correspond to surface Mn^{3+} and Mn^{4+} ions [66]. Mn^{3+}/Mn^{4+} molar ratios of the MnO_2, K/MnO_2, Pt/MnO_2 and $K\text{-}Pt/MnO_2$ catalysts were 0.52, 0.89, 1.00 and 1.08, respectively (Table-1), which means the additional K/Pt makes the catalysts containing more Mn^{3+} ions. The Mn^{3+} /Mn^{4+} ratio of $K\text{-}Pt/MnO_2$ catalyst was larger than those of the other samples, and the possible reason was that the Mn-O bond connection was weakened by the strong interaction within K/Pt and O [67]. In consequence, the content of Mn^{3+} increased alongside the chargeability of Mn atoms. The increase of surface Mn^{3+} ions could enhance the amount of oxygen vacancies[68]. Two signals could also be observed from O 1s spectra showed in Fig. 6B. The bond energy at ~529.7 and ~531.2 eV were according with the O_{latt} and O_{ads}, respectively[62]. Table-1 displayed that the O_{ads} /O_{latt} ratio of $K\text{-}Pt/MnO_2$ (2.00) was larger than the ratio of Pt/MnO_2 (1.67), K/MnO_2 (1.06) and MnO_2 (0.85), which indicates the O_{ads} increases with the additional K/Pt content. This consequence indicated that K/Pt could promote forming active O_{ads} species, verifying the presence of the intense metal–support interaction further, which will discussed in the following section. Literatures had reported[69] that the O_{ads} species made a critical difference in formaldehyde catalytic activity. Because of high activity of the O_{ads} species and the interaction between reactant and catalyst surface, it tended to participate in the oxidation reaction [70,71]. Also, a greater number of surface oxygen vacancies over $K\text{-}Pt/MnO_2$ due to a larger ratio of O_{ads}/O_{latt}, which would provide higher catalytic activity. The K 2p spectra for K/MnO_2 and $K{-}Pt/MnO_2$ was showed in Fig. 6C. It displayed two binding energy at ~292.8 and ~295.6 eV assigned to potassium ions. Through charge transfer from K to oxygen, the electron-rich K atoms were actively favorable for splitting oxygen manifested by the theoretical calculation [74]. The Pauli repulsion was weakened due to sp electrons local migrating to empty d shell, and O atom was allowed to close and get into the chemisorption region [72]. Therefore, higher content of surface adsorbed oxygen in the catalysts which adding postassium was attributed to easier dissociative adsorption of oxygen illustrated by the XPS analysis.

The Raman pattern of the catalysts was displayed in Fig.7. MnO_2 showed a band at 635.2 cm^{-1} according with the symmetric ν2 (Mn−O) stretching vibration of [MnO_6] groups[73]. This was indicated a rutile type structure with the interstitial space. The spectra comparability indicated that the MnO_2 、K/MnO_2、Pt/MnO_2 and $K{-}Pt/MnO_2$ catalysts had the fundamental structure. The weak peak at 349 cm^{-1} was according with skeletal vibrations. With the K/Pt addition, the peaks of K/MnO_2, Pt/MnO_2 and $K\text{-}Pt/MnO_2$ at 635.2cm^{-1} shifted to higher wavenumber at 642, 639 and 644 cm^{-1}, respectively (blue shifts), which indicate the existence of disorder crystal defects or residual stress. The crystal defects were favorable to form oxygen vacancies. This interaction rooted in the effect of surface stress for the surface structure, which may be consistent with TiO_2 sample because of the similar structure with a rutile type[74]. The result further confirmed that a microscopic stress was the reason why (110) peak of K/MnO_2, Pt/MnO_2 and $K\text{-}Pt/MnO_2$ widens with addition of K/Pt. The literature reported that blue shifts and larger peak width can cause the increase of oxygen vacancies. Therefore, the $K\text{-}Pt/MnO_2$ contained stronger interaction between K/Pt and Mn, more oxygen vacancies and lattice defects, which is coincident with the XRD and XPS results. The oxygen vacancies were of advantage to adsorb, activate, and migrate of oxygen in the oxidation reaction of HCHO.

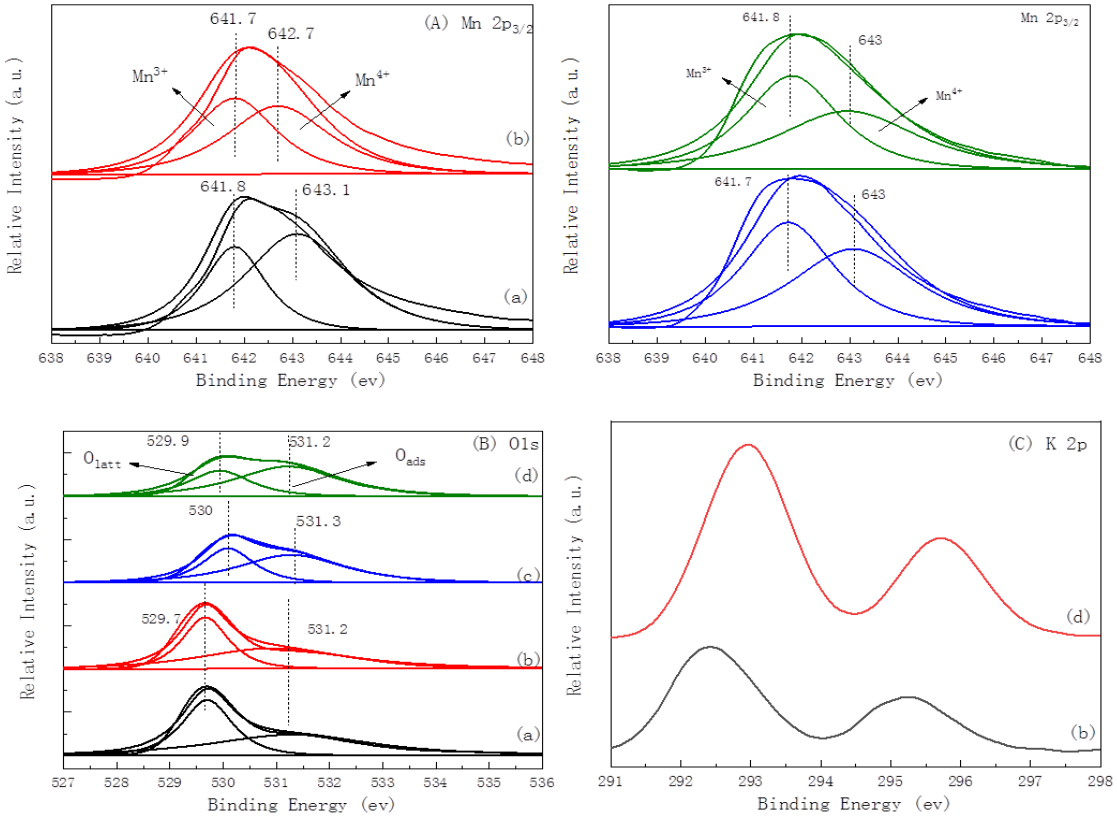

Fig.6. XPS spectra of MnO_2 (a),K/MnO_2 (b), Pt/MnO_2 (c), and K−Pt/MnO_2 (d).

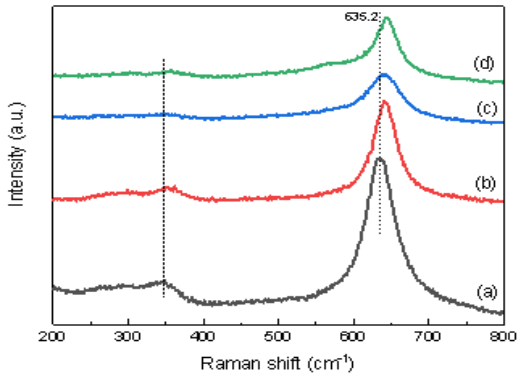

Fig.7: Raman spectra of MnO_2 (a), K/MnO_2 (b), Pt/MnO_2 (c), and K−Pt/MnO_2 (d).

Fig.8(A) studied the reducibility of the samples, and showed H_2-TPR profiles conducting over MnO_2 and K-doped MnO_2 together with the Pt/MnO_2 and the K-doped Pt/MnO_2 catalyst. Because of the existence of a disproportionation reaction, the MnO_2 pattern showed reduction peak 1 at 284°C, peak 2 at 345°C, and peak 3 at 392°C, corresponding to the MnO_2 been reduced to Mn_2O_3, Mn_2O_3 been reduced to Mn_3O_4, and Mn_3O_4 been reduced to MnO, respectively [62]. Three peaks of K/MnO_2 overlapped, of which peak 1 at 249°C, its peak 2 at 275°C, peak 3 at 322°C, corresponding to the reduction reaction just like the MnO_2. It indicated more active lattice oxygen in the K/MnO_2. The reduction profile bearing close and poorly resolved maxima at around 79°C after the additon of Pt on the Pt/MnO_2 samples [75]. The Pt addition could activate surface oxygen of manganese dioxide support, which may desorb and react with formaldehyde at low temperature easily. The reduction peak of PtO transferred to a higher temperature at around 97°C due to the further adding of K- over K-Pt/MnO_2 catalyst with a slight shoulder at about 153°C. The above consequences manifested an interaction of the K- and Pt, which generated the K- stabilized PtO for the catalysts [76]. Table-1 showed the increasing Mn^{3+} /Mn^{4+} mole ratios of the catalysts with the additional of K/Pt, indicating the K/MnO_2, Pt/MnO_2 and K-Pt/MnO_2 had great quantities of Mn^{3+} cations. In addition, Fig 8 showed the Pt/MnO_2 and K-Pt/MnO_2 had much stronger low-temperature reducibility. Therefore, they exhibited excellent catalyic performance for HCHO oxidation.

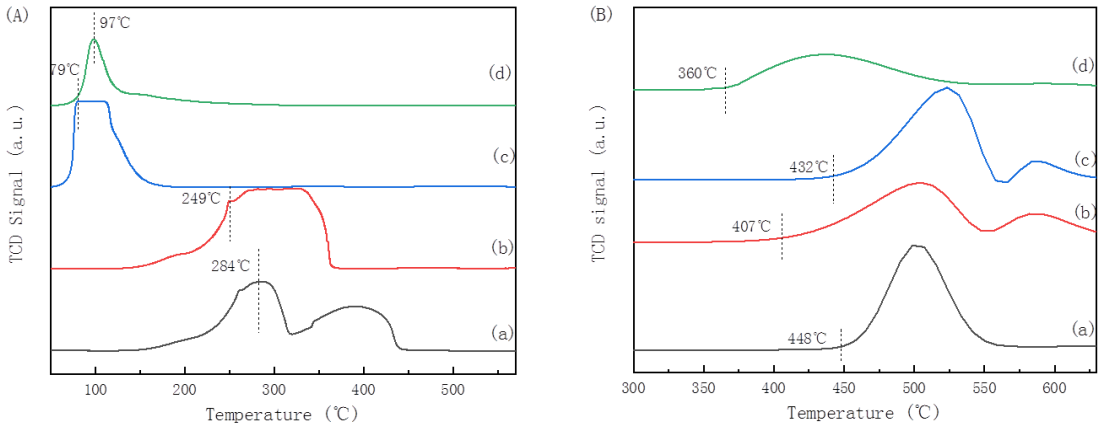

Fig.8: (A) H_2-TPR profiles, (B) O_2-TPO profiles of MnO_2 (a), K/MnO_2 (b), Pt/MnO_2 (c) and K-Pt/MnO_2 (d) catalysts.

Furthermore, for purpose of researching O_2 mobility and activation over the MnO_2 and K/Pt-MnO_2 catalysts, TPO tests were carried out and the consequences were displayed in Fig 8B. As plotted in Fig.8B, the TPO results provided other information on catalysts redox performances. The oxidization began to happen, when the line of K-Pt/MnO_2 started to rise at about 360°C. The highest temperature of oxidization profiles was lay at 435-520°C. Towards MnO_2, K/MnO_2 and Pt/MnO_2, the oxidization signal started at 448°C, 407°C and 432°C, respectively. After K/Pt added, the O_2 desorption peak turned to lower temperatures for K-Pt/MnO_2 and centered at 435 °C, which means additional K/Pt improved the production of the surface-active oxygen species.

Catalytic activity of formaldehyde

Fig 9 showed the HCHO catalytic oxidation performance using various catalysts. With the rise of temperatures, the full conversion of HCHO by MnO_2 catalyst was displayed at 130℃. K/MnO_2 catalyst reached the complete conversion in lower temperature than MnO2 catalyst because of the existence of K^+ ions, which can promote the activation of the oxygen and water joining into HCHO oxidation reaction[77]. The addition of Pt obviously promoted the formaldehyde catalytic oxidation performance. Complete conversion of Pt/MnO_2 was obtained at 9℃. With simultaneous addition of K/Pt content, K-Pt/MnO_2 catalyst showed the best catalytic performance. It achieved almost 100% HCHO conversion at 0℃. There are some similar researches, for example, Lu *et al.*,.[88] synthesized a series of Ag–K/MnO_2 nanorods with various molar ratios of K/Ag. The Ag–K/MnO_2 nanorods with an optimal K/Ag molar ratio of 0.9 showed excellent formaldehyde conversion efficiency of 100% at a low temperature of 60°C and no noticeable decrease in the catalytic activity was found during five on/off cycles (300 ppm HCHO and WHSV of 36000 mL g_{cat}^{-1} h^{-1}). Huang *et al.*,.[89] prepared Pt/MnNi@NF catalyst via in situ hydrothermal growth of manganese dioxide–nickel(II) hydroxide (MnO2–Ni(OH)2) hierarchical nanosheets and subsequent impregnation–borohydride reduction to deposit well-dispersed platinum (Pt) nanoparticles (NPs). Pt/MnNi@NF showed remarkably enhanced HCHO degradation performance with 88% of HCHO removed within 60 min at room temperature (the initial HCHO concentration at around 200 ppm, relative humidity of 50%). Compared with the previous reported catalysts, the K-Pt/MnO_2 catalyst exhibited lower temperature for complete decomposition of formaldehyde. For the synergistic effect between potassium and platinum, Pt is demonstrated to increase the mobility of active substances produced on the alkaline constituent[78,79] and the formation of Pt-O-Mn bonds at interface of Pt/MnO_2 can improve catalysts reducibility. The addition of K/Pt could improve the amount of surface active oxygen species, which might be due to the interface effect between K/Pt and MnO_2 for improving the oxygen activation ability and enhancing lattice oxygen transference from MnO_2 to K-Pt/MnO_2 interface. The spent catalysts were characterized by XRD and XPS, as shown in Fig.10 and Fig.11. The crystalline structures of samples were well preserved after the HCHO conversion. Surface element molar ratio determined by the XPS measurement of the spent catalysts was also shown in Table-2, and the reaction process had no influence on the valence states of Mn species. Besides, the formaldehyde catalytic activity on the basis of time on stream over K-Pt/MnO_2 sample had no remarkable decrease after reacted for 70h. Therefore, the addition of K/Pt significantly improved the formaldehyde oxidation performance.

The conclusions in Table-3 displayed that the RT of different samples. The K-Pt/MnO_2 was more active for formaldehyde oxidation. The samples RT was ranked in the sequence of K-Pt/MnO_2> Pt/MnO_2> K/MnO_2> MnO_2 at the same temperature, which further confirmed that the doping of K/Pt could remarkably improve the formaldehyde catalytic oxidation.

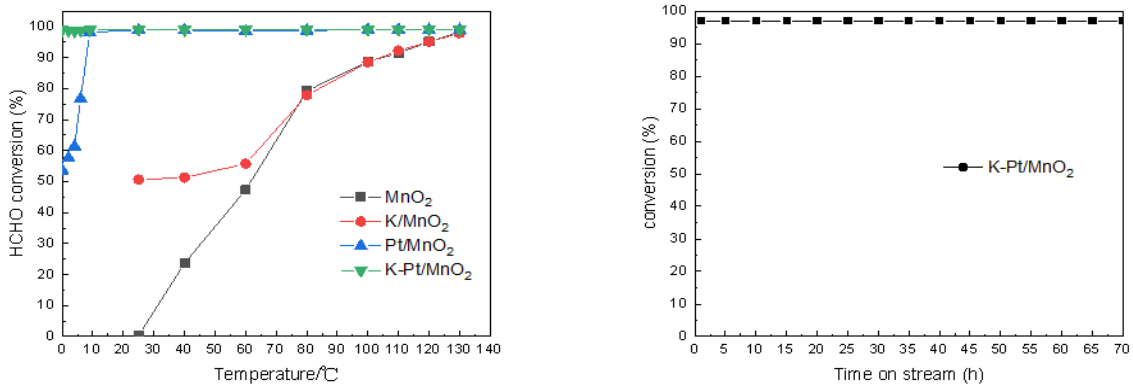

Fig.9: HCHO catalytic activity of the different samples, and the activity with time on stream over K-Pt/MnO_2 catalyst at GHSV of 50,000 ml/(g·h) at 0℃. Reaction conditions: formaldehyde concentration = 20ppm, O_2 (20 vol.%), balance N_2.

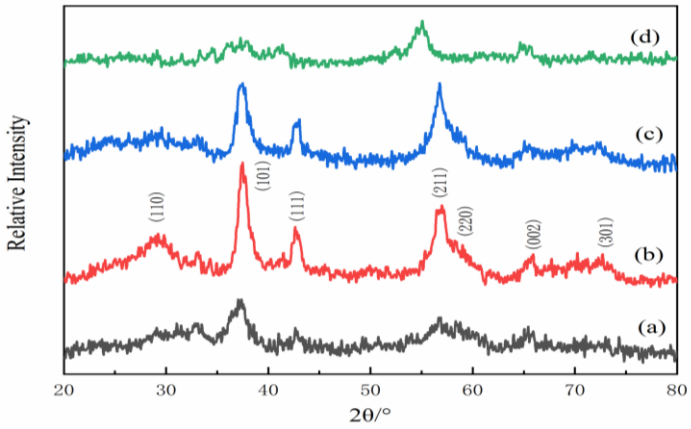

Fig.10. The XRD patterns of the spent MnO_2 (a), K/MnO_2 (b), Pt/MnO_2 (c) and K-Pt/MnO_2 (d).

Table-2: Surface element molar ratio determined by the XPS measurement of the spent catalysts.

Sample	**Surface element molar ratio**	
	Mn^{3+}/Mn^{4+}	**O_{ads}/O_{latt}**
MnO_2	**0.5**	**1**
K/MnO_2	**0.79**	**1.1**
Pt/MnO_2	**1**	**1.4**
K-Pt/MnO_2	**1.1**	**1.6**

Table-3: Reaction rates (RT) of various samples at different temperature for formaldehyde oxidation.

Catalyst	$R_0 \times 10^9$ mol·m^{-2}·s^{-1}	$R_9 \times 10^9$ mol·m^{-2}·s^{-1}	$R_{25} \times 10^9$ mol·m^{-2}·s^{-1}	$R_{60} \times 10^9$ mol·m^{-2}·s^{-1}	$R_{100} \times 10^9$ mol·m^{-2}·s^{-1}	$R_{130} \times 10^9$ mol·m^{-2}·s^{-1}
MnO_2	-	-	142.56	13424.85	22482.45	23042.12
K/MnO_2	-	-	26038.89	25671.42	36386.09	37251.14
Pt/MnO_2	19693.65	34909.68	34909.68	34909.68	34909.68	34909.68
$K\text{-}Pt/MnO_2$	71766.62	71766.62	71766.62	71766.62	71766.62	71766.62

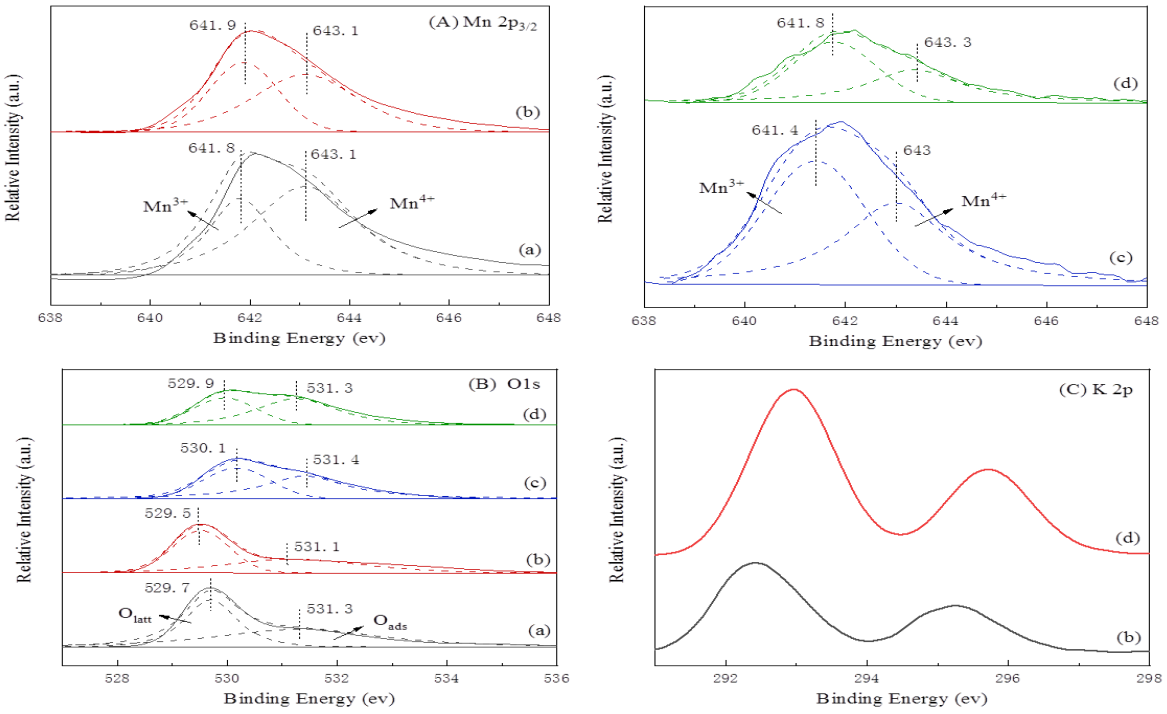

Fig.11: XPS spectra of the spent MnO_2 (a),K/MnO_2 (b), Pt/MnO_2 (c), and $K-Pt/MnO_2$ (d).

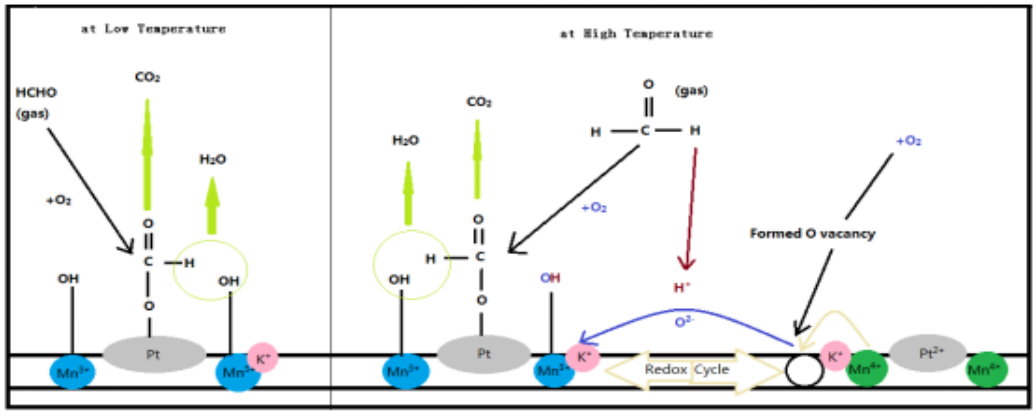

Fig.12. Reaction mechanism of HCHO oxidation over $K\text{-}Pt/MnO_2$ catalyst.

The framework of MnO_2 catalyst had a 3D pore channel structure and large surface area that could conduct to diffusion of reaction gas, products, and the exposure of the active site[40]. According to the characterization analysis, Pt nanoparticles were distributed in the Pt/MnO_2 and $K\text{-}Pt/MnO_2$ sample. The K/Pt addition only reduced the pore size and surface area, but the basic structure was still preserved. Surface adsorbed oxygen and abundant Pt active phase usually existed in the Pt-loaded oxide samples, which can enhance the catalytic performance at low reaction temperature [80,81], while MnO_2 support only acted as a reservoir that provides oxygen species[82]. Based on XPS and H_2 -TPR results, the K/MnO_2, Pt/MnO_2 and $K{-}Pt/MnO_2$ samples possessed more abundant O_{ads}, which were beneficial to adsorb and activate of HCHO molecules. The additional K/Pt changed the distribution of original Mn^{4+} in MnO_2 support and increased the amount of Mn^{3+} ions. A larger Mn^{3+} /Mn^{4+} ratio was useful to the formation of more oxygen vacancies. Raman results also confirmed that $K{-}Pt/MnO_2$ might form sufficient oxygen vacancies because of the maximum structural defects. Therefore, the $K\text{-}Pt/MnO_2$ possessed stronger interaction of K/Pt with Mn, more lattice defects and oxygen vacancies. The oxygen vacancies were benefit to adsorb, activate, and migrate of oxygen in formaldehyde removal. H_2 -TPR profiles verified that the strong interaction between MnO_2 and K/Pt. The added Pt obviously shifted the reduction peaks of MnO_2 to lower oxidation temperatures. Pt/MnO_2 and $K\text{-}Pt/MnO_2$ catalysts had better low-temperature reducibility because of the Pt addition. TPO experiments indicated that the doping of K/Pt improved surface-active oxygen production over the doped MnO_2 samples.

As a matter of fact, K/Pt, Mn^{3+} ions, and O_{ads} species of the $K{-}Pt/MnO_2$ catalyst were all involved in catalytic reaction process. The addition of K/Pt can activate O_{ads} of MnO_2 support. In oxidation process, the active O^{2-} surrounding Pt were depleted and replenished by MnO_2 directly. As plotted in Fig. 12, the redox cycles of Mn^{4+}/Mn^{3+} and Pt^{2+}/Pt^{0} were beneficial to activate and migrate of oxygen on the oxygen vacancies after the O^{2-} species consumed [83,84]. Like the $Na{-}Pt/TiO_2$ sample reaction pathway, a surface OH^- could reacted with formate species immediately on $K{-}Pt/MnO_2$ surface to form CO_2 and H_2O molecules [12]. We believed that the formaldehyde catalytic performance on the $K{-}Pt/MnO_2$ sample was depended on the surface OH^- surrounding of Pt at low oxidation temperature. The surface OH^- were quickly consumed and replaced at relatively high temperature which would supplied by the migration of O^{2-} from MnO_2. The reaction pathway was exhibited clearly in Fig. 12. Therefore, the reaction pathway for formaldehyde catalytic oxidation on $K{-}Pt/MnO_2$ abided by the route of $HCHO \rightarrow CHOO^- + OH^- \rightarrow CO_2 + H_2O$. As Pt/MnO_2, the pathway of reaction abided by the route of $HCHO \rightarrow CHOO^- \rightarrow CO + O^* \rightarrow CO_2$ [41]. In the catalytic oxidation reaction, the O^{2-} species played a key role. Through the occurence of oxygen vacancies, these active O* caused the complex migration frequently [85-87].

Conclusion

In summary, MnO_2, K/MnO_2, Pt/MnO_2 and $K\text{-}Pt/MnO_2$ catalysts with the same structures were successfully synthesized using both hard template method and impregnation method, and the polycrystalline pore walls highly distributed the Pt nanoparticles. The basic mesoporous structure was not affected due to the additional Pt and K^+ ions and merely reduced the surface areas, pore diameters, and pore volumes. The performance degradation of HCHO catalytic oxidation over all these MnO_2 catalysts following the order: $K\text{-}Pt/MnO_2$ > Pt/MnO_2 > K/MnO_2 > MnO_2. Mesoporous $K\text{-}Pt/MnO_2$ catalysts had the optimal catalytic activity for formaldehyde at low temperature because of the interaction of K/Pt with Mn, more Mn^{3+} ions provided by anion lattice defects and more O_{ads} species on the surface. HCHO completely oxidized to CO_2 at 0℃ when the space velocity (GHSV) was $50000h^{-1}$. No degradation of performance was observed after the catalyst was run for 70h. Because of the activity and stability of $K\text{-}Pt/MnO_2$, it exhibited promise for the efficient HCHO removal. We speculated that on $K{-}Pt/MnO_2$ sample, the surface OH^- species surrounding the Pt largely determined the formaldehyde catalytic performance at low temperature; the surface OH^- were quickly consumed and replaced at relatively high temperature, which would supplied by the migration of O^{2-} from MnO_2. The mechanism for the K/Pt-promoted catalytic performance would be better understand through this consequence.

Author Contributions

Conceptualization, Shengnan Guan; Data curation, Shengnan Guan; Formal analysis, Shengnan Guan, Yanyan Lei and Kun Chen; Funding acquisition, Wenzhi Li; Investigation, Shengnan

Guan; Methodology, Wenzhi Li; Project administration, Wenzhi Li; Resources, Wenzhi Li; Software, Jianru Ma; Supervision, Wenzhi Li and Qi Zhang; Writing – original draft, Shengnan Guan; Writing – review & editing, Shengnan Guan, Wenzhi Li and Qingchuan Liu.

Acknowledgements

This study was financially supported by the Science and Technological Fund of Anhui Province for Outstanding Youth (1508085J01), the International Technology Cooperation Plan of Anhui (No. 1503062030) and the National Key Technology R&D Program of China (NO. 2015BAD15B06)

References

1. T. Salthammer, S. Mentese, and R. Marutzky, Formaldehyde in the indoor environment. *CHEM REV*, **110**, 2536 (2010).
2. J.S. Quiroz Torres, J. P. Royer, Bellat, J. M. Giraudon, and J. F. Lamonier, Formaldehyde: catalytic oxidation as a promising soft way of elimination. *ChemSusChem*, **6,** 578 (2013)..
3. X. Tang, J. Chen, X. Huang, Y. Xu, and W. Shen, Pt/MnOx–CeO2 catalysts for the complete oxidation of formaldehyde at ambient temperature. *APPL CATAL B-ENVIRON*, **81**, 115 (2008).
4. S. S. Kim, K. H. Park, and S. C. Hong, A study on HCHO oxidation characteristics at room temperature using a Pt/TiO_2 catalyst. *APPL CATAL A-GEN*, **398**, 96 (2011)..
5. F. Shiraishi, D. Ohkubo, K. Toyoda, and S. Yamaguchi, Decomposition of gaseous formaldehyde in a photocatalytic reactor with a parallel array of light sources: 1. Fundamental experiment for reactor design. *CHEM ENG J*, **114**, 153 (2005).
6. C. H. Ao, and S. C. Lee, Enhancement effect of TiO_2 immobilized on activated carbon filter for the photodegradation of pollutants at typical indoor air level. *APPL CATAL B-ENVIRON*, **44**, 191 (2003)..
7. F. Holzer, U. Roland, and F. D. Kopinke, Combination of non-thermal plasma and heterogeneous catalysis for oxidation of volatile organic compounds: Part 1. Accessibility of the intra-particle volume. *APPL CATAL B-ENVIRON*, **38**, 163 (2002)..
8. G. Zhang, Z. Sun, Y. Duan, R. Ma, and S. Zheng, Synthesis of nano-TiO_2/diatomite composite and its photocatalytic degradation of gaseous formaldehyde. *APPL SURF SCI*, **412**, 105 (2017)..
9. L. Bai, F. Wyrwalski, M. Safariamin, R. Bleta, J. F. Lamonier, C. Przybylski, and A. Ponchel, Cyclodextrin-cobalt (II) molecule-ion pairs as precursors to active Co_3O_4/ZrO_2 catalysts for the complete oxidation of formaldehyde: Influence of the cobalt source. *J CATAL*, **341**, 191 (2016).
10. S. Rong, P. Zhang, Y. Yang, L. Zhu, J. Wang, and F. Liu, MnO_2 framework for instantaneous mineralization of carcinogenic airborne formaldehyde at room temperature. *ACS CATAL*, **7**, 1057 (2017).
11. H. Huang, and D. Y. Leung, Complete elimination of indoor formaldehyde over supported Pt catalysts with extremely low Pt content at ambient temperature. *J CATAL*, **280**, 60 (2011)..
12. C. Zhang, F. Liu, Y. Zhai, H. Ariga, N. Yi, Y. Liu, and H. He, Alkali-metal-promoted Pt/TiO2 opens a more efficient pathway to formaldehyde oxidation at ambient temperatures. *ANGEW CHEM INT EDIT*, **51**, 9628 (2012)..
13. X. Yu, J. He, D. Wang, Y. Hu, H. Tian, and Z. He, Facile controlled synthesis of Pt/MnO2 nanostructured catalysts and their catalytic performance for oxidative decomposition of formaldehyde. *J PHYS CHEM C*, **116**, 851 (2011)..
14. Y. Shen, X. Yang, Y. Wang, Y. Zhang, H. Zhu, L. Gao, and M. Jia, The states of gold species in CeO_2 supported gold catalyst for formaldehyde oxidation. *APPL CATAL B-ENVIRON*, **79**, 142 (2008).
15. H. F. Li, N. Zhang, P. Chen, M. F. Luo, and J. Q. Lu, High surface area Au/CeO_2 catalysts for low temperature formaldehyde oxidation. *APPL CATAL B-ENVIRON*, **110**, 279 (2011).
16. B. Liu, C. Li, Y. Zhang, Y. Liu, W. Hu, Q. Wang, and J. Zhang, Investigation of catalytic mechanism of formaldehyde oxidation over three-dimensionally ordered macroporous Au/CeO_2 catalyst. *APPL CATAL B-ENVIRON*, **111**, 467 (2012).
17. C. Ma, D. Wang, W. Xue, B. Dou, H. Wang, and Z. Hao, Investigation of formaldehyde oxidation over Co_3O_4–CeO_2 and Au/Co_3O_4–CeO_2 catalysts at room temperature: effective removal and determination of reaction mechanism. *ENVIRON SCI TECHNOL*, **45**, 3628 (2011).
18. B. Liu, Y. Liu, C. Li, W. Hu, P. Jing, Q. Wang, and J. Zhang, Three-dimensionally ordered macroporous Au/CeO_2-Co_3O_4 catalysts with

nanoporous walls for enhanced catalytic oxidation of formaldehyde. *APPL CATAL B-ENVIRON*, **127**, 47 (2012).

19. A. Yusuf, C. Snape, J. He, H. Xu, C. Liu, M. Zhao, and S. N. Behera, Advances on transition metal oxides catalysts for formaldehyde oxidation: A review. *CATAL REV*, **59**, 189 (2017).
20. J. Wang, J. Li, C. Jiang, P. Zhou, P. Zhang, and J. Yu, The effect of manganese vacancy in birnessite-type MnO2 on room-temperature oxidation of formaldehyde in air. *APPL CATAL B-ENVIRON*, **204**, 147 (2017).
21. X. Q. Deng, X. Zhu, Z. G. Sun, X. S. Li, J. L. Liu, C. Shi, and A. M. Zhu, Exceptional activity for photocatalytic mineralization of formaldehyde over amorphous titania nanofilms. *CHEM ENG J*, **306**, 1001 (2016).
22. Y. Zheng, W. Wang, D. Jiang, and L. Zhang, Amorphous MnOx modified Co_3O_4 for formaldehyde oxidation: improved low-temperature catalytic and photothermocatalytic activity. *CHEM ENG J*, **284**, 21 (2016).
23. M. Wiechen, I. Zaharieva, H. Dau, and P. Kurz, Layered manganese oxides for water-oxidation: alkaline earth cations influence catalytic activity in a photosystem II-like fashion. *CHEM SCI*, **3**, 2330 (2012)..
24. A. Wang, H. Wang, H. Deng, S. Wang, W. Shi, Z. Yi, R. Qiu, and K. Yan, Controllable synthesis of mesoporous manganese oxide microsphere efficient for photo-Fenton-like removal of fluoroquinolone antibiotics. *APPL CATAL B-ENVIRON*, **248**, 298 (2019).
25. R. Li, Y. Liu, H. Li, M. Zhang, Y. Lu, L. Zhang, J. Xiao, F. Boehm, and K. Yan, One-Step Synthesis of NiMn-Layered Double Hydroxide Nanosheets Efficient for Water Oxidation. *Small Methods*, **3**, 1800344，(2019).
26. Y. Sekine, Oxidative decomposition of formaldehyde by metal oxides at room temperature. *ATMOS ENVIRON*, **36**, 5543 (2002).
27. J. Xiao, and T. Frauenheim, Activity and Synergy Effects on a Cu/ZnO (000 1) Surface Studied Using First-Principle Thermodynamics. *J PHYS CHEM LETT*, **3**, 2638 (2012).
28. X. Zhang, H. Wang, and B. Q. Xu, Remarkable nanosize effect of zirconia in Au/ZrO2 catalyst for CO oxidation. *J PHYS CHEM B*, **109**, 9678 (2005).
29. L. Liu, X. Gu, Y. Cao, X. Yao, L. Zhang, C. Tang, and L. Dong, Crystal-plane effects on the catalytic properties of Au/TiO_2. *ACS CATAL*, **3**, 2768 (2013).
30. Z. Yan, Z. Xu, B. Cheng, and C. Jiang, Co_3O_4 nanorod-supported Pt with enhanced performance for catalytic HCHO oxidation at room temperature. *APPL SURF SCI*, **404**, 426 (2017).
31. M. Wang, L. Zhang, W. Huang, Y. Zhou, H. Zhao, J. Lv, and J. Shi, Pt/MnO_2 nanosheets: facile synthesis and highly efficient catalyst for ethylene oxidation at low temperature. *RSC ADV*, **7**, 14809 (2017).
32. X. Yu, J. He, D. Wang, Y. Hu, H. Tian, and Z. He, Facile controlled synthesis of Pt/MnO_2 nanostructured catalysts and their catalytic performance for oxidative decomposition of formaldehyde. *J PHYS CHEM C*, **116**, 851 (2011).
33. J. Ye, X. Zhu, B. Cheng, J. Yu, and C. Jiang, Few-layered graphene-like boron nitride: a highly efficient adsorbent for indoor formaldehyde removal. *ENVIRON SCI TECH LET*, **4**, 20 (2016).
34. Z. Yan, Z. Xu, J. Yu, and M. Jaroniec, Effect of microstructure and surface hydroxyls on the catalytic activity of Au/AlOOH for formaldehyde removal at room temperature. *J COLLOID INTERF SCI*, **501**, 164 (2017).
35. Y. Li, C. Zhang, H. He, J. Zhang, and M. Chen, Influence of alkali metals on Pd/TiO_2 catalysts for catalytic oxidation of formaldehyde at room temperature. *CATAL SCI TECHNOL*, **6**, 2289 (2016)..
36. Y. Li, C. Zhang, and H. He, Significant enhancement in activity of Pd/TiO_2 catalyst for formaldehyde oxidation by Na addition. *CATAL TODAY*, **281**, 412 (2017).
37. L. Nie, J. Yu, X. Li, B. Cheng, G. Liu, and M. Jaroniec, Enhanced performance of NaOH-modified Pt/TiO_2 toward room temperature selective oxidation of formaldehyde. *ENVIRON SCI TECHNOL*, **47**, 2777 (2013)..
38. G. Avgouropoulos, E. Oikonomopoulos, D. Kanistras, and T. Ioannides, Complete oxidation of ethanol over alkali-promoted Pt/Al2O3 catalysts. *APPL CATAL B-ENVIRON*, **65**, 62 (2006)..
39. J. Hou, L. Liu, Y. Li, M. Mao, H. Lv, and X. Zhao, Tuning the K^+ concentration in the tunnel of OMS-2 nanorods leads to a significant enhancement of the catalytic activity for benzene oxidation. *ENVIRON SCI*

TECHNOL, **47**, 13730 (2013).
40. C. Zhang, Y. Li, Y. Wang, and H. He, Sodium-promoted Pd/TiO_2 for catalytic oxidation of formaldehyde at ambient temperature. *ENVIRON SCI TECHNOL*, **48**, 5816 (2014).
41. B. Bai, and J. Li, Positive effects of K+ ions on three-dimensional mesoporous Ag/Co_3O_4 catalyst for HCHO oxidation. *ACS CATAL*, **4**, 2753 (2014).
42. B. Bai, H. Arandiyan, and J. Li, Comparison of the performance for oxidation of formaldehyde on nano-Co_3O_4, 2D-Co_3O_4, and 3D-Co_3O_4 catalysts. *APPL CATAL B-ENVIRON*, **142**, 677 (2013).
43. B. Lee, D. Lu, J. N. Kondo, and K. Domen, Three-dimensionally ordered mesoporous niobium oxide. *J AM CHEM SOC*, **124**, 11256 (2002).
44. Y. Ren, Z. Ma, and P. G. Bruce, Ordered mesoporous metal oxides: synthesis and applications. *CHEM SOC REV*, **41**, 4909 (2012).
45. F. Jiao, A. H. Hill, A. Harrison, A. Berko, A. V. Chadwick, and P. G. Bruce, Synthesis of ordered mesoporous NiO with crystalline walls and a bimodal pore size distribution. *J AM CHEM SOC*, **130**, 5262 (2008).
46. K. Jiao, B. Zhang, B. Yue, Y. Ren, S. Liu, S. Yan, and He, H. Growth of porous single-crystal Cr 2 O 3 in a 3-D mesopore system. *CHEM COMMUN*, **45**, 5618 (2005).
47. H. Tüysüz, C. W. Lehmann, H. Bongard, B. Tesche, R. Schmidt, and F. Schüth, Direct imaging of surface topology and pore system of ordered mesoporous silica (MCM-41, SBA-15, and KIT-6) and nanocast metal oxides by high resolution scanning electron microscopy. *J AM CHEM SOC*, **130**, 11510 (2008).
48. T. Xingfu, X. HUANG, S. Jianjun, L. I. U. Junlong, L. I. Yonggang, X. U. Yide, and S. H. E. N. Wenjie, Synthesis and catalytic performance of manganese oxide octahedral molecular sieve nanorods for formaldehyde oxidation at low temperature. *CHINESE J CATAL*, **27**, 97 (2006).
49. *An, N., Yu, Q., Liu, G., Li, S., Jia, M. and Zhang, W.* Complete oxidation of formaldehyde at ambient temperature over supported Pt/Fe2O3 catalysts prepared by colloid-deposition method. *J HAZARD MATER*, *186*, 1392 (2011).
50. N. An, W. Zhang, X. Yuan, B. Pan, G. Liu, M. Jia, and W. Zhang, Catalytic oxidation of formaldehyde over different silica supported platinum catalysts. *CHEM ENG J*, **215**, 1 (2013).
51. A. Rumplecker, F. Kleitz, E. L. Salabas, and F. Schüth, Hard templating pathways for the synthesis of nanostructured porous Co3O4. *CHEM MATER*, **19**, 485 (2007)..
52. J. Y. Luo, Y. G. Wang, H. M. Xiong, and Y. Y. Xia, Ordered mesoporous spinel LiMn2O4 by a soft-chemical process as a cathode material for lithium-ion batteries. *CHEM MATER*, **19**, 4791 (2007)..
53. F. Jiao, and P. G. Bruce, Mesoporous Crystalline β-MnO2—a Reversible Positive Electrode for Rechargeable Lithium Batteries. *ADV MATER*, **19**, 657 (2007)..
54. B. Lee, D. Lu, J. N. Kondo, and K. Domen, Three-dimensionally ordered mesoporous niobium oxide. *J AM CHEM SOC*, **124**, 11256 (2002)..
55. H. Tüysüz, C. W. Lehmann, H. Bongard, B. Tesche, R. Schmidt, and F. Schüth, Direct imaging of surface topology and pore system of ordered mesoporous silica (MCM-41, SBA-15, and KIT-6) and nanocast metal oxides by high resolution scanning electron microscopy. *J AM CHEM SOC*, **130**, 11510 (2008).
56. F. Jiao, A. Harrison, J. C. Jumas, A. V. Chadwick, W. Kockelmann, and P. G. Bruce, Ordered mesoporous Fe_2O_3 with crystalline walls. *J AM CHEM SOC*, **128**, 5468 (2006).
57. J. Y. Luo, Y. G. Wang, H. M. Xiong, and Y. Y. Xia, Ordered mesoporous spinel $LiMn_2O_4$ by a soft-chemical process as a cathode material for lithium-ion batteries. *CHEM MATER*, **19**, 4791 (2007).
58. F. Jiao, J. C. Jumas, M. Womes, A. V. Chadwick, A. Harrison, and P. G. Bruce, Synthesis of ordered mesoporous Fe_3O_4 and γ-Fe_2O_3 with crystalline walls using post-template reduction/oxidation. *J AM CHEM SOC*, **128**, 12905 (2006).
59. K. Jiao, B. Zhang, B. Yue, Y. Ren, S. Liu, S. Yan, and H. He, Growth of porous single-crystal Cr_2O_3 in a 3-D mesopore system. *CHEM COMMUN*, **45**, 5618 (2005).
60. B. Bai, J. Li, and J. Hao, 1D-MnO_2, 2D-MnO_2 and 3D-MnO_2 for low-temperature oxidation of ethanol. *APPL CATAL B-ENVIRON*, **164**, 241 (2015).
61. W. Gac, The influence of silver on the structural, redox and catalytic properties of the cryptomelane-type manganese oxides in the low-temperature CO oxidation reaction. *APPL CATAL B-ENVIRON*, **75**, 107 (2007).
62. L. Nie, A. Meng, J. Yu, and M. Jaroniec, Hierarchically macro-mesoporous Pt/γ-Al_2O_3

composite microspheres for efficient formaldehyde oxidation at room temperature. *SCI REP-UK*, **3**, 3215 (2013).

63. P. Zhou, X. Zhu, J. Yu, and W. Xiao, Effects of adsorbed F, OH, and Cl ions on formaldehyde adsorption performance and mechanism of anatase TiO2 nanosheets with exposed {001} facets. *ACS APPL MATER IN*, **5**, 8165 (2013).
64. Z. Xu, J. Yu, G. Liu, B. Cheng, P. Zhou, and X. Li, Microemulsion-assisted synthesis of hierarchical porous $Ni(OH)_2/SiO_2$ composites toward efficient removal of formaldehyde in air. *DALTON T*, **42**, 10190 (2013).
65. C. M. Julien, M. Massot, and C. Poinsignon, Lattice vibrations of manganese oxides: Part I. Periodic structures. *SPECTROCHIM ACTA A*, **60**, 689 (2004).
66. Q. Ye, J. Zhao, F. Huo, D. Wang, S. Cheng, T. Kang, and H. Dai, Nanosized Au supported on three-dimensionally ordered mesoporous β-MnO_2: Highly active catalysts for the low-temperature oxidation of carbon monoxide, benzene, and toluene. *MICROPOR MESOPOR MAT*, **172**, 20(2013)..
67. J. Wang, J. Li, P. Zhang, and G. Zhang, Understanding the "seesaw effect" of interlayered K+ with different structure in manganese oxides for the enhanced formaldehyde oxidation. *APPL CATAL B-ENVIRON*, **224**, 863 (2018)..
68. F. Wang, H. Dai, J. Deng, G. Bai, K. Ji, and Y. Liu, Manganese oxides with rod-, wire-, tube-, and flower-like morphologies: highly effective catalysts for the removal of toluene. *ENVIRON SCI TECHNOL*, **46**, 4034-4041 (2012)..
69. B. B. Chen, X. B. Zhu, M. Crocker, Y. Wang, and C. Shi, FeOx-supported gold catalysts for catalytic removal of formaldehyde at room temperature. *APPL CATAL B-ENVIRON*, **154**, 73 (2014).
70. M. Setvín, U. Aschauer, P. Scheiber, Y. F. Li, W. Hou, M. Schmid, and U. Diebold, Reaction of O_2 with subsurface oxygen vacancies on TiO_2 anatase (101). *SCIENCE*, **341**, 988 (2013).
71. G. I. Panov, K. A. Dubkov, and E. V. Starokon, Active oxygen in selective oxidation catalysis. *CATAL TODAY*, **117**, 148 (2006).
72. F. Xu, Z. Huang, P. Hu, Y. Chen, L. Zheng, J. Gao, and X. Tang, The promotion effect of isolated potassium atoms with hybridized orbitals in catalytic oxidation. *CHEM COMMUN*, **51**, 9888 (2015).
73. K. Rout, M. Mohapatra, and S. Anand, A critical analysis of cation adsorption from single and binary solutions on low surface area β-MnO_2. *APPL SURF SCI*, **270**, 205 (2013).
74. C. Lejon, and L. Österlund, Influence of phonon confinement, surface stress, and zirconium doping on the Raman vibrational properties of anatase TiO_2 nanoparticles. *J RAMAN SPECTROSC*, **42**, 2026 (2011)..
75. H. Zhu, Z. Qin, W. Shan, W. Shen, and J. Wang, Pd/CeO_2–TiO_2 catalyst for CO oxidation at low temperature: a TPR study with H_2 and CO as reducing agents. *J CATAL*, **225**, 267 (2004)..
76. X. Zhu, M. Shen, L. L. Lobban, and R. G. Mallinson, Structural effects of Na promotion for high water gas shift activity on Pt–Na/TiO_2. *J CATAL*, **278**, 123 (2011)..
77. P. Hu, Z. Amghouz, Z. Huang, F. Xu, Y. Chen, and X. Tang, Surface-confined atomic silver centers catalyzing formaldehyde oxidation. *ENVIRON SCI TECHNOL*, **49**, 2384 (2015).
78. R. Matarrese, L. Castoldi, L. Lietti, and P. Forzatti, Soot combustion: Reactivity of alkaline and alkaline earth metal oxides in full contact with soot. *CATAL TODAY*, **136**, 11 (2008)...
79. K. Krishna, and M. Makkee, Soot oxidation over NOx storage catalysts: Activity and deactivation. *Catalysis Today*, **114**, 48 (2006)..
80. Z. Huang, X. Gu, Q. Cao, P. Hu, J. Hao, J. Li, and X. Tang, Catalytically Active Single-Atom Sites Fabricated from Silver Particles. *ANGEW CHEM*, **124**, 4274 (2012).
81. C. F. Mao, and M. A. Vannice, Formaldehyde oxidation over Ag catalysts. *J CATAL*, **154**, 230 (1995).
82. R. Xu, X. Wang, D. Wang, K. Zhou, and Y. Li, Surface structure effects in nanocrystal MnO_2 and Ag/MnO_2 catalytic oxidation of CO. *J CATAL*, **237**, 426 (2006).
83. X. Xie, Y. Li, Z. Q. Liu, M. Haruta, and W. Shen, Low-temperature oxidation of CO catalysed by Co 3 O 4 nanorods. *NATURE*, **458**, 746 (2009)..
84. G. G. Xia, Y. G. Yin, W. S. Willis, J. Y. Wang, and S. L. Suib, Efficient stable catalysts for low temperature carbon monoxide oxidation. *J CATAL*, **185**, 91 (1999).
85. A. Wittstock, V. Zielasek, J. Biener, C. M. Friend, and M. Bäumer, Nanoporous gold catalysts for selective gas-phase oxidative coupling of methanol at low temperature. *SCIENCE*, **327**, 319 (2010).
86. H. Over, and A. P. Seitsonen, Oxidation of metal surfaces. *SCIENCE*, **297**, 2003 (2002).
87. Y. Lei, F. Mehmood, S. Lee, J. Greeley, B. Lee, S. Seifert, and D. Teschner, Increased silver

activity for direct propylene epoxidation via subnanometer size effects. *SCIENCE*, **328**, 224 (2010).

88. S. Lu, X. Wang, Q. Zhu, C. Chen, X. Zhou, Huang and F. Pang, Ag–K/MnO_2 nanorods as highly efficient catalysts for formaldehyde oxidation at low temperature. *RSC ADV*, **8**, .

14221, (2018).

89. S. Huang, B. Cheng, J. Yu, and C. Jiang, Hierarchical Pt/MnO_2–$Ni(OH)_2$ Hybrid Nanoflakes with Enhanced Room-Temperature Formaldehyde Oxidation Activity. *ACS SUSTAIN CHEM ENG*, **6**, 12481, (2018).